nature communications

Article

https://doi.org/10.1038/s41467-025-62909-1

Wide temperature range adaptable electric field driven binder for advanced lithium-sulfur batteries

Received: 26 January 2025

Accepted: 5 August 2025

Published online: 23 August 2025

Check for updates

Wanyuan Jiang[1], Xin Jin[2], Borui Li[2], Yunpeng Qu[2], Lin Wang[2], Ce Song[3], Mengfan Pei[2], Tianpeng Zhang[4] ✉, Xigao Jian[1,2] ✉ & Fangyuan Hu[2] ✉

Stable operation over wide temperature ranges is still a great challenge for lithium-sulfur batteries facing actual operating environments. Electrocatalysis is an effective strategy to address the sluggish reaction kinetics of lithium polysulfides at low temperatures and exacerbated shuttling effect at high temperatures; however, its practicality is still restricted by the structural stability of the support electrodes. In this work, a binder with wide temperature range adaptability is designed with a structure-modulated stable electrocatalytic mechanism, which can achieve effective adsorption and accelerated conversion of lithium polysulfides, and high-temperature self-repair and low-temperature internal support of electrodes. Lithium-sulfur batteries with the binder have a specific capacity of 780 mAh g^{-1} (5 C, 8375 mA g^{-1}), and 470 mAh g^{-1} (0.1 C, 167.5 mA g^{-1}) even at −40 °C. This work realizes the stable operation across a temperature range of 100 °C solely by the innovative development of binder, which provides a unique perspective for wide-temperature range lithium-sulfur battery design.

Lithium-sulfur (Li||S) batteries, with high specific energy of 2600 Wh kg^{-1} and theoretical specific capacity of 1675 mAh g^{-1}, as well as high raw material sulfur abundance, are extremely promising for a new generation of energy storage devices[1–3]. In order to address the inherent problems, such as sluggish reaction kinetics, shuttle effect, and electrode volume expansion due to multistep reaction mechanism and the diverse nature of sulfur species[4–9], numerous studies have been conducted at room temperature, achieving significant performance improvements. However, limited research has explored the behavior and performance of these batteries in high- or low-temperature environments. Facing the complex and variable operating environment of practical situations, it is necessary for energy storage devices to work stably in wide temperature ranges[10–12].

For electrochemical reactions involving 16 electron transitions from S_8 molecules to insoluble Li_2S in Li||S batteries, low-temperature environments would exacerbate the slow reaction kinetics of the rate-determining step (the conversion from higher-order lithium polysulfides (LiPSs) to Li_2S_2/Li_2S[13,14]), leading to the accumulation of soluble LiPSs and severe hindrance of the solid phase conversion reaction[15–17]. Although high temperature environments can accelerate the rate-determining step, the increased solubility of LiPSs in electrolyte will further exacerbate the shuttling effect, leading to a drastic decrease in battery stability[18–20]. Electrocatalytic strategies can

[1]State Key Laboratory of Fine Chemicals, Frontiers Science Center for Smart Materials Oriented Chemical Engineering, School of Chemical Engineering, Technology Innovation Center of High Performance Resin Materials (Liaoning Province), Dalian University of Technology, Dalian, China. [2]School of Materials Science and Engineering, State Key Laboratory of Fine Chemicals. Frontiers Science Center for Smart Materials Oriented Chemical Engineering, Technology Innovation Center of High Performance Resin Materials (Liaoning Province), Dalian University of Technology, Dalian, China. [3]Science and Technology on Advanced Ceramic Fiber and Composites Laboratory, College of Aerospace Science and Engineering, National University of Defense Technology, Changsha, China. [4]Key Laboratory of Bio-based Material Science and Technology (Ministry of Education), College of Materials Science and Engineering, Northeast Forestry University, Harbin, PR China. ✉e-mail: zhangtp@nefu.edu.cn; jian4616@dlut.edu.cn; hufangyuan@dlut.edu.cn

https://doi.org/10.1038/s41467-025-62909-1

effectively accelerate reaction kinetics and reduce the accumulation and shuttling of LiPSs. Accordingly, various electrocatalysts have been proposed and shown great potential in enhancing the electrochemical properties of Li||S batteries[21–25]. As a unique electrocatalyst, liquid metal (LM) has high electrical conductivity, good mobility, a certain degree of adhesion, as well as self-healing properties[26,27]. More importantly, compared to non-homogeneous electrocatalysts with fixed catalytic sites and homogeneous redox mediators prone to shuttle losses, liquid metal can accelerate Li||S electrochemical reaction kinetics more efficiently by providing dynamic catalytic sites at the active interface of LiPSs reactions[28–30]. However, the utility of supported LM catalysts depends heavily on LM dispersion uniformity and loading stability[31]. Thus, the practical application of LM in Li||S batteries is limited by the instability of electrode structure originated from the positive electrode volume expansion. While binders, as the intrinsic components of electrodes, not only play a crucial role in stabilizing electrode structures[32–37], but also have great potential to adsorb and catalyze LiPSs, thereby enhancing the reaction kinetics of Li||S batteries[37]. Therefore, the development of novel polymer binders with stable catalytic activity is of great significance for improving the structural and electrochemical stability of Li||S batteries across a wide temperature range.

Herein, this study proposes a structure-modulated stable electrocatalytic strategy through designing a composite binder (GSCC) composed of short conjugated segments modified polymers based on natural macromolecules and gallium-tin liquid metal possessing dynamic catalytic sites. The potential of GSCC as a wide-temperature-range adaptive binder is also investigated in temperature range of −40 °C to 60 °C. During the cycling of Li||S batteries, the short conjugated segments in GSCC provide higher local electronic conductivity, while the coordination of polar groups combined with the electric-field-driven nature of LM ensures a homogeneous and stable electrocatalytic environment. The high mechanical properties of the binder provide favorable structural stability, leading to higher electrocatalytic performance (Fig. 1a). Furthermore, both electrochemical impedance (EIS) tests and Li_2S nucleation tests over a wide temperature range show that GSCC-based batteries exhibit stable reaction kinetics at the rate-determining step, even under high/low temperature conditions. The results demonstrate that Li||S batteries with GSCC binder have a discharge specific capacity of 780 mAh g^{-1} at a high current of 5 C (8.37 A g^{-1}), and retain 470 mAh g^{-1} at −40 °C. Even at a high temperature of 60 °C after 600 h, the average capacity decay rate per cycle is only 0.095%. In addition, the pouch cell with GSCC binder has 870 mAh g^{-1} reversible specific capacity after cycles at a E/S ratio of 7 μL mg^{-1}. This study presents a stable electrocatalytic strategy −achieved solely through binder innovation−to achieve stable Li||S battery performance across the 100 °C range, providing a unique perspective for the wide temperature range design of Li||S batteries.

Results

Synthesis and characterization of GSCC binders

GSCC consists of gallium-tin liquid metal and caffeic acid modified chitosan (CC), synthesized via a cell pulverization-freeze drying process, in which the polymer component CC is obtained from the natural polymer chitosan (CTS) and the biobased monomer caffeic acid (CA) by an amidation reaction at 25 °C. Nuclear magnetic resonance tests (NMR) were 10conducted to demonstrate the successful preparation of CC. As shown in Supplementary Fig. 1, the signal peaks shown in the ^{1}H NMR spectra of CC at about 7.55–6.20 ppm corresponded to the carbon-carbon double bond and the H1-H5 proton on the catechol structure of CA, whereas the signal peaks shown at 3.98–1.96 ppm are attributed to the CTS protons and acetylated functional group residues, which proves the successful grafting of CA[38]. Besides, the functional group structure in CC was further demonstrated by Fourier transform infrared spectroscopy (FTIR). The signal peaks of carbonyl group and C=C are observed at 1635 cm^{-1} and 1605 cm^{-1}, respectively, while the signal peak of the benzene ring in the catechol structure is shown at 1523 cm^{-1} (Supplementary Fig. 2), demonstrating the

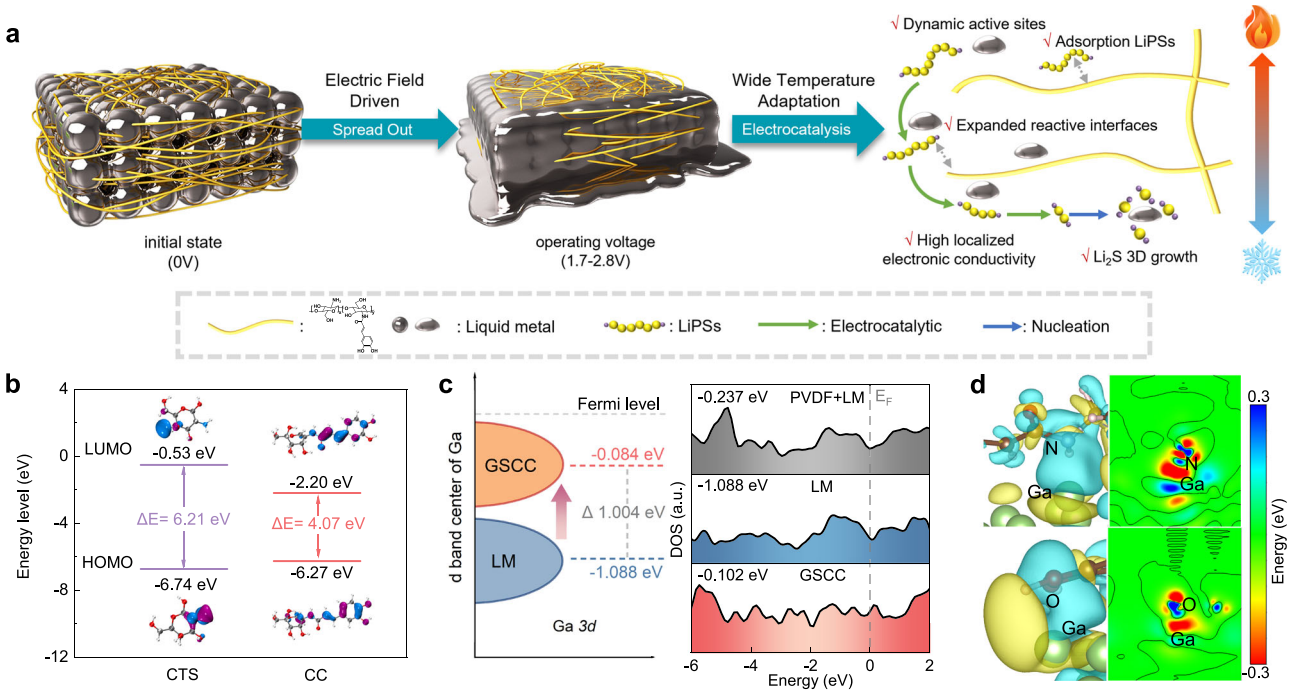

Fig. 1 | Schematic illustration of GSCC and the structural advantages of polymers in GSCC. a Schematic illustration of GSCC binder's electric field driving characteristics at volt-free and Li||S battery operating voltages, and the advantages of GSCC-based Li||S batteries over wide operating temperature ranges. **b** Calculated HOMO and LUMO energy levels of CTS and CC. **c** The *d*-band center of the *3 d* orbital of Ga atoms in pure LM and GSCC binders and density of states for pure LM, LM + PVDF, and GSCC, E_F indicates the Fermi energy level (**d**) Differential charge density modeling and slicing diagram for GSCC. (Blue corresponds to the charge depletion region and red corresponds to the charge accumulation region.).

structure of short conjugated segments in CC. The chemical environment of gallium-tin liquid metal in GSCC was examined with X-ray photoelectron spectroscopy (XPS). Ga^0 and Ga^{3+} appear at 1142.5 eV (1116.1 eV) and 1144.1 eV (1117.7 eV), respectively, while Sn^0 and Sn^{4+} appear at 494.8 eV (487.1 eV) and 492.3 eV (483.9 eV), respectively, indicating that the gallium-tin liquid metal interacts with O-containing groups to form a minor oxide layer (Supplementary Fig. 3)[39,40]. Scanning electron microscope (SEM) and transmission electron microscope (TEM) test images demonstrate that GSCC shows a fluffier structure that stabilizes the loading of LM particles and promotes its uniform distribution (Supplementary Figs. 4 and 5). To further demonstrate the enhancement of integral electrocatalytic performance by polymer and LM complexation in GSCC, a series of theoretical calculations were carried out. Introducing the conjugated structure leads to a decrease in the energy gap[41] and an increase in the localized electronic conductivity. Comparing the Highest Occupied Molecular Orbital (HOMO) and Lowest Unoccupied Molecular Orbital (LUMO) energy levels of CC with unmodified CTS shows that the energy gap decreases from 6.21 eV in CTS to 4.07 eV in CC (Fig. 1b and Supplementary Data 1), consistent with the electronic conductivity test results (Supplementary Fig. 6).

By calculating the d band center (Fig. 1c and Supplementary Data 2), the center of the 3 d orbital of Ga in GSCC is significantly lower compared to pure LM, indicating stronger interfacial electron transfer kinetics and higher electrochemical activity. Further comparison of the p-band centers of O in CC and GSCC (Supplementary Fig. 7) reveals that the p-band center of the polymer in GSCC shifts downward, indicating that the polymer polar groups coordinate with the LM. Density of states (DOS) calculations (Fig. 1c) for GSCC, pure LM, and Poly (vinylidene fluoride) (PVDF) + LM demonstrate that the polymer-LM composite in GSCC increases the DOS near the Fermi energy level, thereby improving the conductivity and electrocatalytic activity of the overall material[42–44]. In addition, the projected density of states (PDOS) results of CC and GSCC bound to polysulfides (Supplementary Fig. 8) indicate that the coordination of liquid metals with polymers effectively enhances the orbital hybridization and improves the adsorption capacity of GSCC with polysulfides. The differential charge density indicates the electron transfer between polymer structure and LM in GSCC (Fig. 1d and Supplementary Data 3), and the lone pairs of electrons on hydroxyl O and amide N atoms in GSCC facilitate their coordination with Ga and Sn atoms possessing empty orbitals, thus enhancing the electron density at dynamic catalytic sites in GSCC[45].

To evaluate binder's mechanical properties for electrode preparation[5], shear rheology experiments, and oscillatory rheology experiments were conducted (Supplementary Figs. 9 and 10). The results indicate that the viscosity of GSCC-based electrode slurry is close to CC, much higher than that of CTS, and exhibits shear-thinning nature. This indicates that GSCC possesses good electrode-bonding ability and mechanical processability under high-speed stirring. The higher modulus at the same oscillatory strain and the higher oscillatory strain corresponding to the intersection of storage-loss modulus curves further demonstrate that GSCC electrode slurries can form mechanically stronger elastic networks and maintain elastic-dominated rheological behavior over a wider strain range. Swelling tests were employed to probe the swelling resistance of different binders (Supplementary Fig. 11). Compared to PVDF, GSCC exhibits favorable swelling resistance, and this contributes to maintaining the electrode structure stability. In addition, the mechanical strength of GSCC-based electrodes was further characterized by nanoindentation tests (Supplementary Fig. 12). GSCC-based electrodes were able to withstand much higher external forces than PVDF-based electrodes at the same indentation depths, and the Young's modulus and hardness were higher than those of PVDF at the maximum indentation depths, proving the ability of GSCC binder to stabilize electrode structures.

Adsorption and electrocatalytic kinetics of GSCC on LiPSs

With the enhanced ability of GSCC to adsorb LiPSs and accelerate the redox kinetics, a series of electrochemical measurements were executed to investigate the adsorption and electrocatalytic kinetics of GSCC binders. Cyclic voltammetry (CV) tests at scan rates of 0.1–0.5 mV s^{-1} were performed to investigate the redox kinetics of LiPSs on various binder-based electrodes. Batteries with GSCC binders exhibited the lower polarization voltage of 317 mV (between oxidation peak a1 and reduction peak c2, corresponding to the rate-determining step), the higher peak current, and the optimal peak voltage (Supplementary Fig. 13). In addition, comparing the Tafel slopes, batteries with GSCC binders exhibited the lowest Tafel slopes (92.3, 44.0, and 33.6 mV dec^{-1}) for both oxidation and reduction processes of S, demonstrating that GSCC can effectively enhance the redox kinetics of LiPSs. The CV contour plots (Fig. 2a–c) indicate that the GSCC-based batteries exhibited stable peak voltages and favorable reversibility at various scan rates, and remained significant current response as the scan rate decreased. The lithium-ion diffusion coefficient (DLi^+) was measured using the Galvanostatic Intermittent Titration Technique (GITT) as shown in the Supplementary Fig. 14. Based on Fick's second law, the D_{Li^+} values of different batteries during charging/discharging processes were calculated (Fig. 2d, e). The results show that the Li^+ diffusion rate of the battery with GSCC binder is better than the batteries with CTS and PVDF, indicating that GSCC can enhance the kinetics of ion transport mechanism in the batteries. CV tests on symmetric batteries were employed to further evaluate the redox kinetics of soluble LiPSs on electrodes with different binders (Supplementary Fig. 15), and the optimal redox peaks of GSCC at identical voltage scanning rates confirmed its improvement on the reaction kinetics of soluble sulfur species.

Enhancing adsorption of LiPSs can effectively suppress the shuttle effect. In the adsorption experiments (Supplementary Fig. 16), the absorption peak intensity in Ultraviolet–visible (UV–vis) spectra of the solution after adsorption by GSCC binder is much lower than that of PVDF binder adsorption, confirming GSCC's stronger adsorption ability on LiPSs. This result is also supported by the LiPSs signal peaks exhibited by the GSCC binder in the XPS test after adsorption experiments. In situ Raman spectroscopy was used to probe GSCC's ability to modulate the shuttling effect of LiPSs in depth. During the discharge of PVDF-based electrodes, strong signal peaks attributed to S_8^{2-} (at 151, 217, and 471 cm^{-1}) were detected on the lithium metal negative electrode side at the beginning of the discharge. As the discharge process proceeded, signal peaks attributed to S_6^{2-} (397 cm^{-1}) and S_4^{2-} + S_5^{2-} (437 cm^{-1}) appeared sequentially (Fig. 2f), indicating the presence of severe LiPSs shuttling in the electrodes using PVDF binder[44,46]. In contrast, only few signals corresponding to S_6^{2-} were detected on the lithium metal negative electrode side during the discharge process of GSCC-based electrodes (Fig. 2g), demonstrating the enhanced adsorption of LiPSs by GSCC binder is effective in mitigating the shuttle effect, which can enhance the cycle stability of batteries. The theoretical adsorption sites of polysulfides on GSCC were analyzed by Bader charge calculations (Supplementary Figs. 17 and 18). The theoretical structures of LiPSs adsorbed on GSCC and PVDF were optimized by density functional theory (DFT) calculations. The adsorption energies and Gibbs free energies of S_8 to Li_2S were calculated. The calculated results demonstrated the strong adsorptions of GSCC for different sulfur species, which were significantly better than those of PVDF (Fig. 2g, Supplementary Fig. 19). It is also in agreement with the results of Bader charge quantification analysis (Supplementary Fig. 20 and Supplementary Table 1), adsorption experiments, and in situ Raman tests. Moreover, during the lithiation of S_8, GSCC unit has a negative Gibbs free energy barrier (−4.88 eV), indicating a spontaneous reaction process. The free energy barriers between various sulfur species of the GSCC unit are all weak during the transition from soluble LiPSs to Li_2S. In particular, for the rate-determining step

https://doi.org/10.1038/s41467-025-62909-1

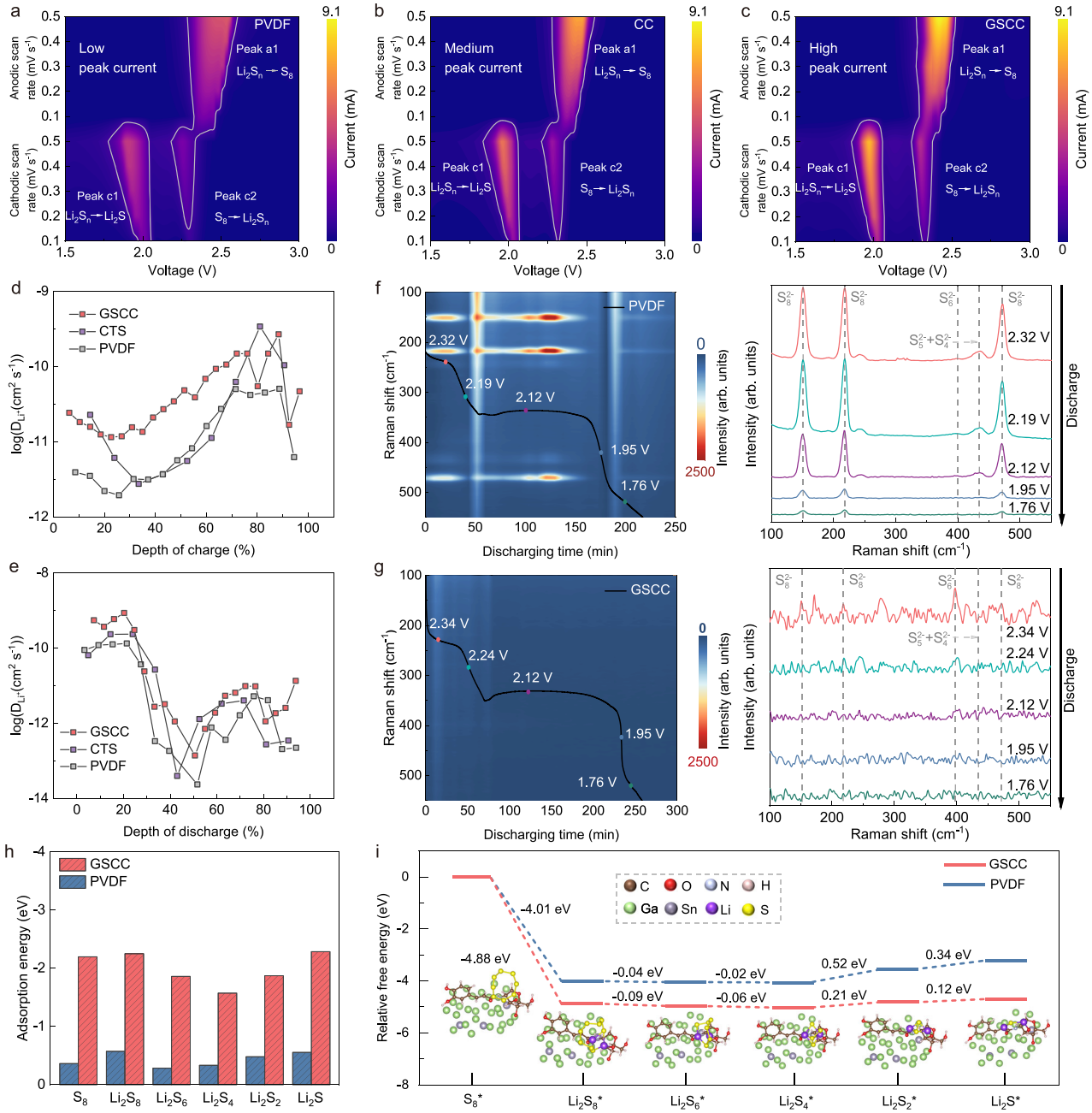

Fig. 2 | Electrochemical tests, spectral characterizations and calculation simulations of active sulfur species on different binders. a–c Contour plots of CV patterns of Li||S batteries with GSCC binder in the 0.1–0.5 mV s^{-1} scan rate range. The calculations of Li^+ diffusion coefficients at different voltages during (**d**) charging. and **e** discharging. In situ Raman spectra of battery with (**f**) PVDF and **g** GSCC binder during discharging at 0.2 C (335 mA g^{-1}) and the corresponding contour maps (Both color scales are 0–2500). **h** Adsorption energies of PVDF and GSCC for various sulfur species (S_8 to Li_2S). **i** Gibbs free energy diagrams for the conversion of S_8 to Li_2S based on electrodes with different binders, inset illustrates the optimized adsorption configurations of GSCC with different sulfur species.

Li_2S_4–Li_2S_2, the free energy difference of the GSCC unit is 0.21 eV, much lower than that of PVDF (0.52 eV), confirming further that GSCC can effectively accelerate the electrochemical reaction kinetics of Li||S batteries.

The electrochemical performances of Li||S batteries with GSCC

The electrodes based on different binders were assembled into Li||S batteries for electrochemical performance measurements to verify the practical effect of the electrocatalytic effect of GSCC binders in the batteries. Figure 3a shows the galvanostatic charge/discharge curves of batteries with different binders at 0.2 C (335 mA g^{-1}, 1 C = 1675 mA g^{-1}). The specific capacity of batteries with GSCC (1188.8 mAh g^{-1}) is significantly higher than that of CC (1118.3 mAh g^{-1}), CTS (970.2 mAh g^{-1}), and PVDF (936.8 mAh g^{-1}) cells and has the lowest polarization voltage. The rate performance test (Fig. 3b) exhibited the improved rate performance of GSCC batteries with discharge specific capacities of 1221.4, 988.2, 920.2, 872.4, 842.2, 820.6, and 792.7 mAh g^{-1} at 0.2 C, 0.5 C, 1 C, 2 C, 3 C, 4 C, and 5 C, respectively. The galvanostatic charge/discharge curves at various currents with stable plateau potentials (Supplementary Fig. 21). Internal resistance of the batteries during charging and discharging was further investigated using the GITT (Fig. 3c and Supplementary Fig. 13). GSCC consistently exhibited low internal resistance during charging and discharging, especially in the activation and nucleation stages of Li_2S. This is

https://doi.org/10.1038/s41467-025-62909-1

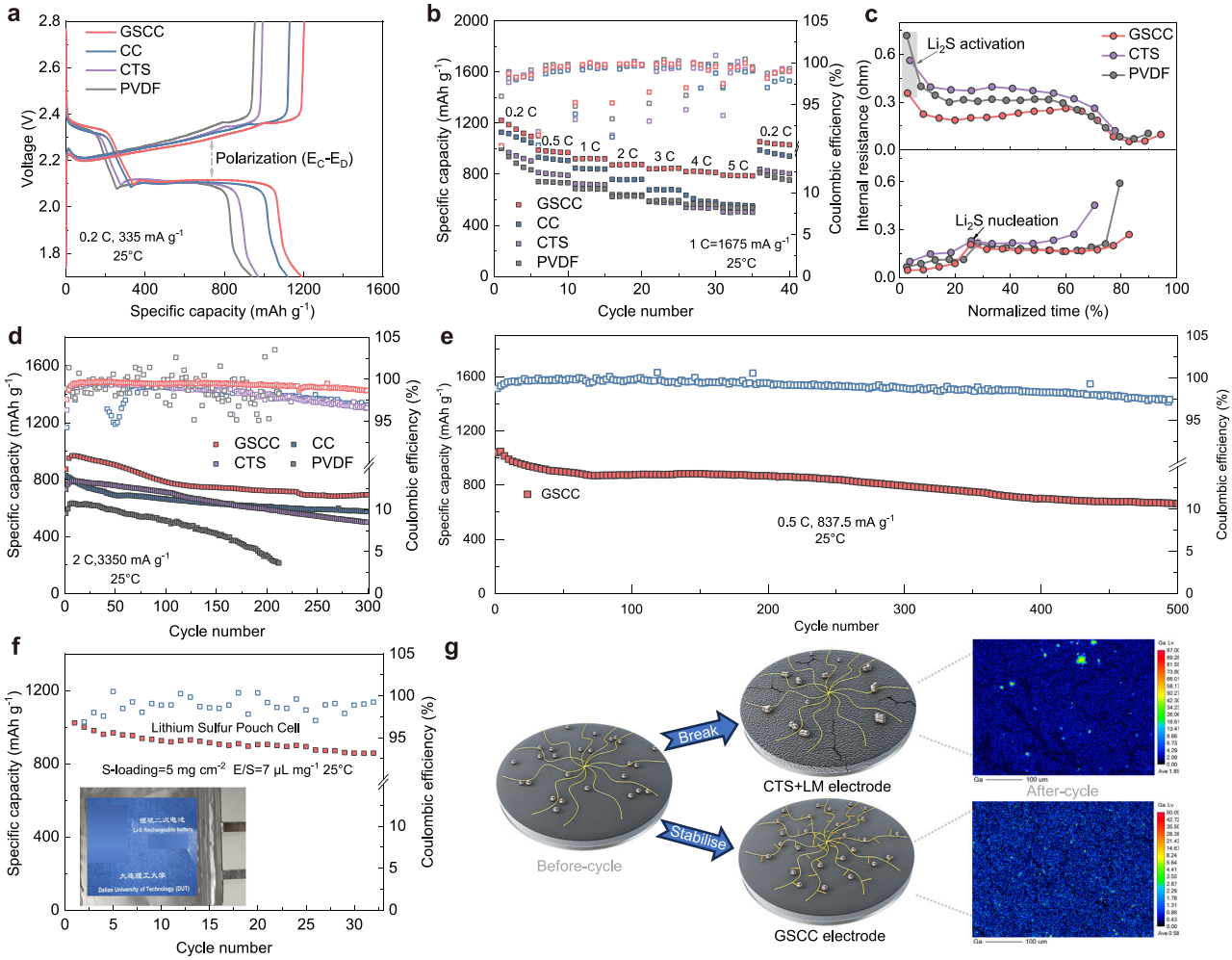

Fig. 3 | Electrochemical performance of Li||S coin batteries and pouch cells based on GSCC binder (Test temperature: 25 °C, 1 C = 1675 mA g^{-1}). **a** Galvanostatic charge-discharge curves for Li||S batteries with different binders at 0.2 C (335 mA g^{-1}). **b** Rate performance different batteries. **c** Internal resistance of different binder-based batteries fitted by GITT test results. **d** Cycle performance of batteries with different binders at 2 C (3350 mA g^{-1}). (**e**) Cycle performance of the GSCC batteries at 0.5 C (837.5 mA g^{-1}). **f** Cycling performance of lithium-sulfur pouch batteries with GSCC binder. **g** Schematic of electrodes based on CTS + LM binder and GSCC binder before and after cycling, and surface scans for EPMA testing of elemental Ga therein.

attributed to the electrocatalytic effect of GSCC and the high electronic conductivity of the LM[47]. The long-term cycling stability is crucial for the practical application of Li||S batteries. Comparing the capacity of electrodes based on various binders after 300 cycles at 2 C (3350 mA g^{-1}, Fig. 3d), the capacity retention of GSCC electrodes is much higher than that of CC, CTS, and PVDF electrodes. Moreover, the Li||S batteries with GSCC binder exhibited high cycling stability over 500 cycles at 0.5 C (837.5 mA g^{-1}, Fig. 3e), with an average capacity decay rate of only 0.072% per cycle, which was attributed to the adsorption-electrocatalytic ability of GSCC to reduce LiPSs accumulation and shuttling.

Nowadays, high sulfur loading and low E/S ratio are gradually becoming key indicators for evaluating Li||S batteries' potential for actual applications. Hence, Li||S batteries with high sulfur loading and relatively less electrolyte were tested. With a sulfur surface loading of 5.7 mg cm^{-2} and a E/S ratio of 6, the GSCC batteries exhibited favorable cycling performance with a specific capacity of 840 mAh g^{-1} at 0.1 C after 30 cycles (Supplementary Fig. 22). Furthermore, GSCC binder-based electrodes were assembled into Li||S pouch cells to verify their electrochemical performance in scale-up measurements and demonstrate their potential for practical application. With a sulfur surface loading of 5 mg cm^{-2} and an E/S ratio of 7, the GSCC binder-based Li||S pouch cell exhibited an initial specific capacity of 1022.6 mAh g^{-1} at 0.1 C and a reversible capacity of 870 mAh g^{-1} after 32 cycles (Fig. 3f), demonstrating that the GSCC binder designed through the stable electrocatalytic strategy remains favorable electrochemical performance under scaled-up conditions, promising to be utilized in practical Li||S batteries. In addition, we explored the ability of GSCC binder to stabilize the electrode structure and electrocatalytic environment through elemental scanning analysis by Electron Probe Microanalysis (EPMA) test and SEM. As shown in Fig. 3g and Supplementary Figs. 23 and 24, both GSCC electrodes and CTS + LM electrodes (with the same liquid metal content) had uniform Ga and S elemental distribution before cycling. While GSCC electrodes exhibited a more homogeneous distribution of LM (Ga) and active materials (S) after cycling, which indicates that the modified polymer CC has a stronger affinity for LM compared to unmodified CTS, thus promoting a homogeneous distribution and reducing its tendency to aggregate into clusters. Supplementary Fig. 25 reveals that the electrode with GSCC shows a flatter and more stable morphology after cycling compared to the composite electrode with CTS and equal amount of LM, which is attributed to the repairing effect of GSCC on electrode microcracks. XPS tests were used to further probe the interaction of the polymer with LM in GSCC (Supplementary Fig. 26). The XPS test

https://doi.org/10.1038/s41467-025-62909-1

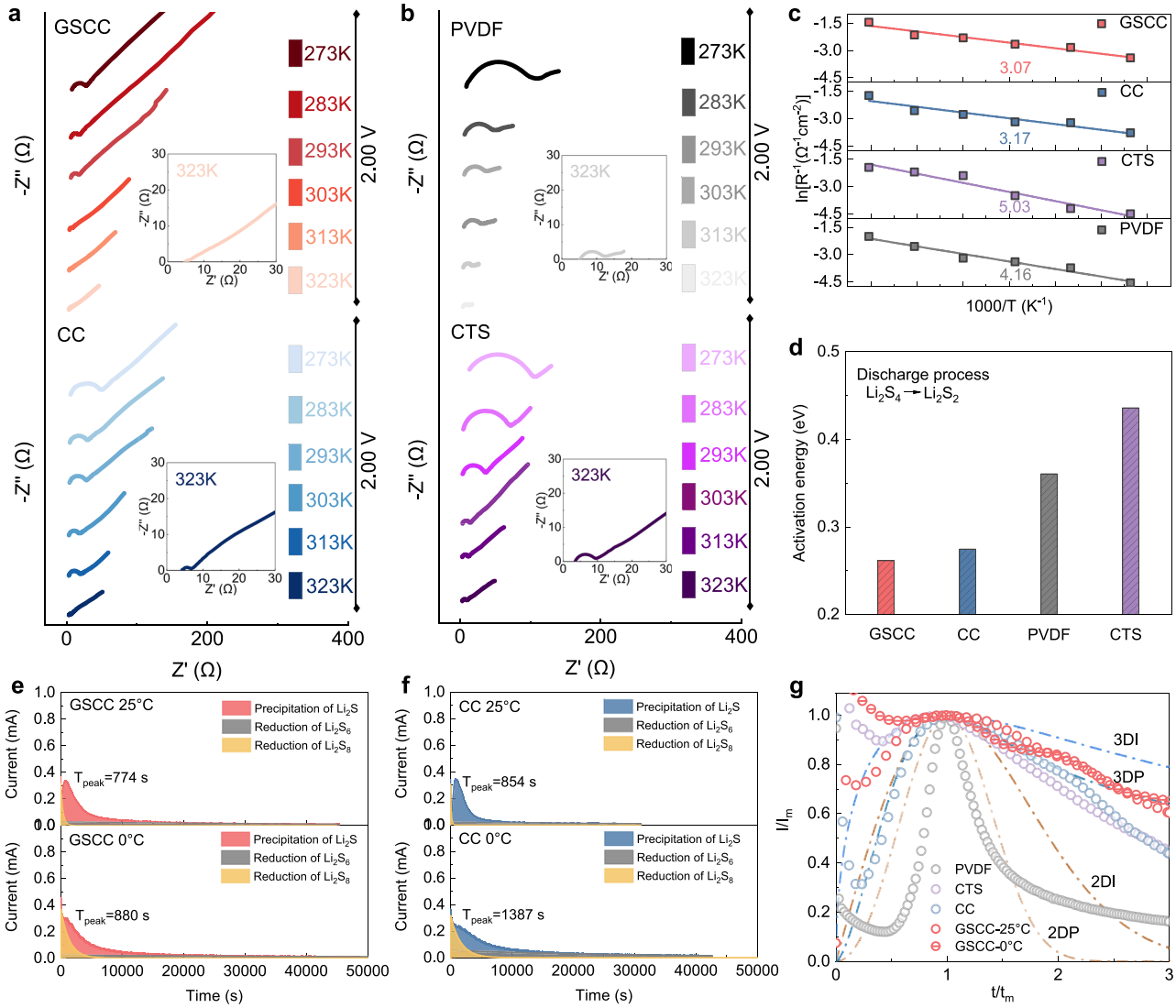

Fig. 4 | Electrochemical performance and kinetic analysis of Li||S batteries with different binders over a wide temperature range. EIS tests of batteries with (**a**) GSCC, CC, **b** CTS, and PVDF binders at different temperatures at 2.0 V. **c** Linear plot of the reciprocal of absolute temperature versus the logarithm of the reciprocal of R_{ct}. **d** The activation energy of batteries based on different binders during the reduction of Li_2S_4 to Li_2S_2. Potentiostatic discharge profiles of Li_2S nucleation on (**e**) GSCC and **f** PVDF based electrodes respectively at 25 °C and 0 °C. **g** Li_2S nucleation model on electrodes with different binders according to theoretical 2D and 3D models.

results indicated a negative shift in the binding energy of the Ga^{3+}3 d peak (−0.31 eV) and a significantly higher ratio of Ga^{3+}/Ga^0 peak area for GSCC as compared to the pure LM, suggesting that the polymer structure provides Ga^{3+} with an electron-rich coordination environment while stabilizing the oxide layer, which can inhibit its aggregation to some extent. In conclusion, the results further elucidate the stable electrocatalytic mechanism of GSCC and demonstrate its practical advantages in improving Li||S batteries electrochemical performance.

Since the electrochemical energy storage mechanism of Li||S batteries is relatively sensitive to temperature[11,12,19,48]. Whether the redox kinetics of LiPSs and the battery electrochemical properties can maintain efficiently over a wide temperature range deserves further investigation. In the sulfur reduction reaction (SRR) of Li||S batteries, the conversion of S_8 to LiPSs is relatively easier, whereas the conversion from LiPSs to insoluble Li_2S_2/Li_2S involves more difficult liquid-solid and solid-solid transformations. Low temperatures pose a greater challenge to the sluggish reaction kinetics of the process. Therefore, the reaction kinetics of the rate-determining step of Li_2S_4 to Li_2S_2 over a wide range of temperatures was emphasized to address the most serious reaction kinetics problem in SRR process. Li||S batteries with various binders were discharged to 2.0 V (corresponding to the conversion of Li_2S_4 to Li_2S_2) and the charge transfer resistance (R_{ct}) of the batteries in different temperature environments were obtained by electrochemical impedance (EIS) measurements (Figs. 4a, b and Supplementary Fig. 27). The EIS plot indicates that the R_{ct} is strongly influenced by the temperature, which decreases significantly with increasing temperature (from 273 K to 323 K) and is much higher than room-temperature R_{ct} at the low temperature of 273 K. This corresponds to the sluggish reaction kinetics of LiPSs resulting from the reduced electrolyte mobility under low-temperature conditions. Significantly, GSCC showed the lowest R_{ct} at different temperatures, and its value varied less (Supplementary Fig. 28), indicating that its electrocatalytic performance and high electronic conductivity advantages accelerate the interfacial charge transfer and improve the reaction kinetics. In addition, a linear relationship exists between the reciprocal of the absolute temperature and the logarithm of the reciprocal of R_{ct} at corresponding temperature (Fig. 4c)[44], from which the activation energy Ea for the conversion step of Li_2S_4 to Li_2S_2 can be deduced according to the Arrhenius formula. The activation energy derivation results (Fig. 4d) show that GSCC batteries have the lowest Ea (0.26 eV)

https://doi.org/10.1038/s41467-025-62909-1

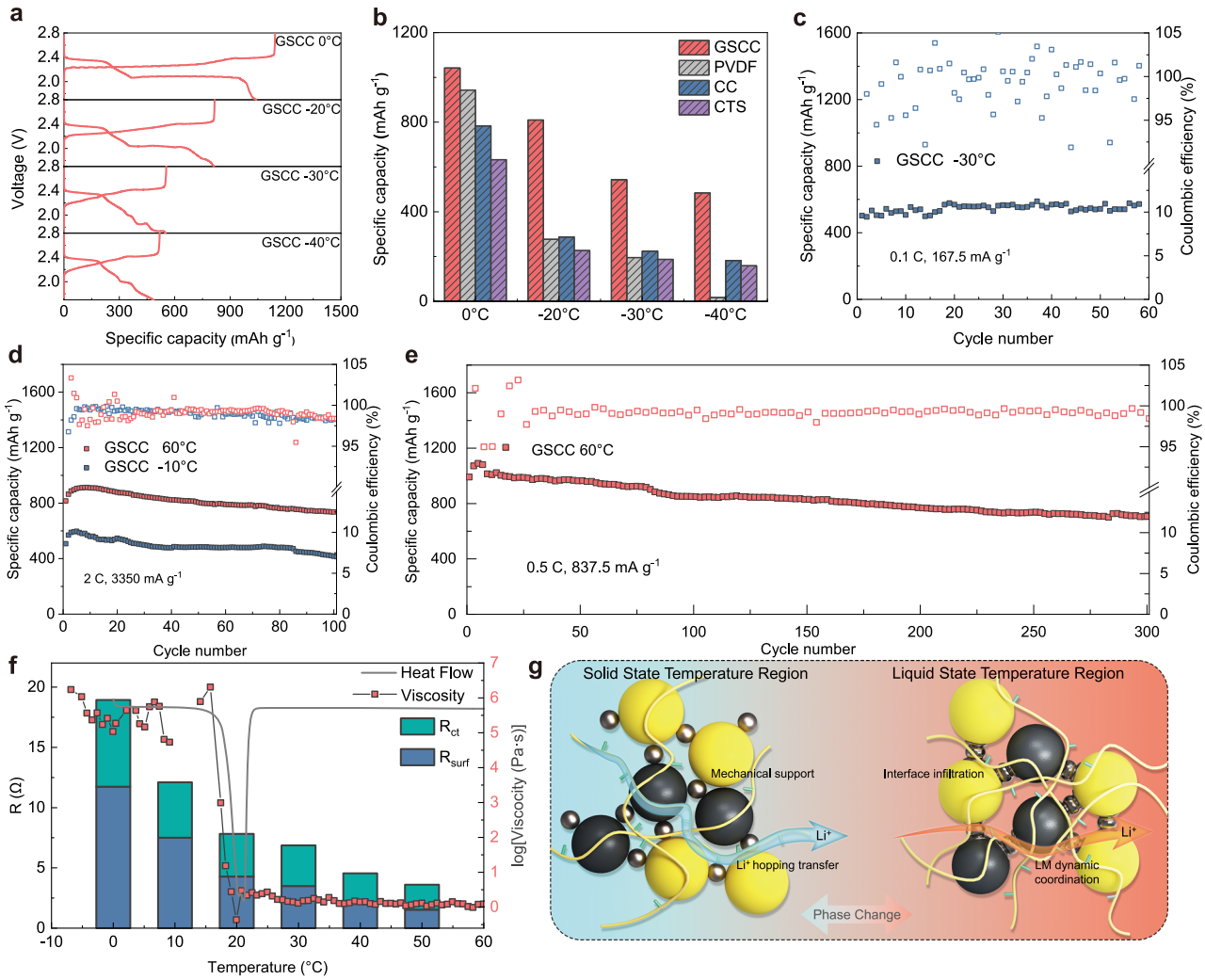

Fig. 5 | Cycling performance of GSCC batteries over a wide temperature range and comparison of operating temperatures (1 C = 1675 mA g^{-1}). a Galvanostatic charge-discharge curves of GSCC electrodes under various temperatures. **b** The specific capacity of Li||S batteries with different binders at 0, −20, −30, and −40 °C at 0.1 C. **c** Cycle performance of GSCC batteries at −30 °C. **d** Cycle performance of GSCC batteries at 2 C (3350 mA g^{-1}) under 60 °C and −10 °C. **e** Cycle performance of GSCC-based batteries at 60 °C. **f** Temperature-Phase-State-Performance linkage analysis plot. **g** Schematic of GSCC operating mechanism in different phase intervals of LM.

and are significantly lower than CC (0.28 eV), CTS (0.36 eV), and PVDF (0.44 eV) batteries, demonstrating that GSCC binders are still effective in improving the reaction kinetics of the rate-determining step in SRR process, even over a wide temperature range.

Constant potentiostatic nucleation tests of Li_2S on electrodes with different binders were executed under 25 °C and 0 °C low-temperature conditions to further reveal the modulating effect of GSCC on the nucleation and precipitation forms of Li_2S. Under 25 °C, the specific capacity corresponding to Li_2S precipitation process on GSCC electrodes was 274.9 mAh g^{-1}, which was much higher than that of CC (213.2 mAh g^{-1}), CTS (68.9 mAh g^{-1}), and PVDF (67.2 mAh g^{-1}) electrodes. GSCC peak time of Li_2S nucleation reaction was the shortest (Fig. 4e, f and Supplementary Figs. 29 and 30). Furthermore, even at the low temperature of 0 °C, the reaction peak time of GSCC electrodes was only delayed by 106 s, attributing to the enhancement of Li_2S nucleation reaction kinetics by the stable and efficient electrocatalytic ability of GSCC in wide temperature range. In order to investigate the Li_2S nucleation mode, the constant potentiostatic nucleation test curves based on different electrodes were fitted and analyzed using the Scharifker-Hills model, in which 3DI and 3DP denote the instantaneous nucleation model and the progressive nucleation model of Li_2S in three-dimensional deposition mode, respectively. Whereas 2DI and 2DP correspond to the instantaneous model and the progressive model of two-dimensional deposition of Li_2S, respectively. Figure 4g shows that the GSCC binder induces a more homogeneous and stable three-dimensional progressive nucleation of Li_2S over a wide temperature range, preventing the two-dimensionally deposited Li_2S from covering the active sites, further indicating that the dynamic active sites provided by GSCC maintain the ability to construct a stable electrocatalytic environment over a wide temperature interval.

We investigated the actual electrical performance of GSCC batteries within -40°C to 60°C. The sluggishness of the reaction kinetics for the rate-determining step is further amplified in low-temperature environments, leading to elevated polarization voltages and shortened or even disappeared discharge plateaus at low potentials. Figure 5a and Supplementary Fig. 31 exhibit the galvanostatic charge-discharge curves of batteries with different binders from −40 °C to 0 °C. At 0.1 C (167.5 mA g^{-1}) the GSCC batteries exhibited 1042.0 mAh g^{-1} (0 °C), 813.4 mAh g^{-1} (−20 °C), 551.1 mAh g^{-1} (−30 °C) and 486.4 mAh g^{-1} (−40 °C) discharge specific capacities, respectively (Fig. 5b). Moreover, even at the low temperature of −40 °C, GSCC batteries still exhibited a clear discharge plateau (corresponding to the conversion of LiPSs to Li_2S_2/Li_2S) and high coulombic efficiency at 2.0 V, compared to other batteries with completely disappeared low-potential discharge

plateau, fully proving their enhanced redox reaction kinetics of LiPSs. For the cycling performance test at −30 °C, 0.1 C, GSCC batteries showed no capacity degradation after 60 cycles (Fig. 5c), and still had a discharge specific capacity of 563 mAh g^{-1}, exhibiting a stable electrocatalytic performance under the low-temperature extreme environments. The cycling performance in −10 °C and 60 °C environments under 2 C (3350 mA g^{-1}, Fig. 5d) was tested to further demonstrate the operational stability of GSCC batteries under high currents in a wide temperature range. After 100 cycles, the GSCC batteries still possessed 735.7 mAh g^{-1} (60 °C) and 416.7 mAh g^{-1} (−10 °C) reversible capacity.

In high-temperature environment, the reaction kinetics of Li||S batteries enhances while the polarization decreases. The increased solubility and accelerated molecular motion in electrolyte leads to a severe exacerbation in the shuttle effect of LiPSs, which is manifested in decreased capacity retention and shortened cycling life of the batteries. The cycling performance of GSCC batteries in high-temperature environment of 60 °C is shown in Fig. 5e. After 300 cycles at 0.5 C (837.5 mA g^{-1}), GSCC still has a reversible capacity of 706.6 mAh g^{-1} with an average capacity decay rate of 0.095% per cycle. The favorable cycling performance in high-temperature environments is attributed to GSCC's adsorption catalytic effect on LiPSs, which effectively reduces the accumulation and shuttling of LiPSs. Further comparing the operating temperature range of this work with some literatures[11,49–52], it is demonstrated that the wide temperature range (100 °C) of GSCC batteries is well competitive (Supplementary Fig. 32).

In the operating temperature range, the GSCC binder not only exhibits great electrochemical performance but also shows favorable high/low temperature and voltage stability (Supplementary Figs. 33–36). To further decouple the working mechanisms of polymer and LM in GSCC over a wide temperature range, Temperature-Phase-State-Performance linkage analysis plots were constructed (Fig. 5f). Based on the results of differential scanning calorimetry (DSC) and viscosity rheology tests, the GSCC binder-based batteries were categorized into solid zone (−40–15 °C), phase change zone (15–25 °C) and liquid zone (25–60 °C) according to the phase change of LM. In the low-temperature region, the metal presents solid property, which mainly serves as a rigid skeleton to provide mechanical support to the electrode structure and inhibit the volume expansion of the electrode. The loss of dynamic properties at this region leads to an increase in the interfacial impedance, but this in turn reduces the aggregation of LM. The low-temperature SEM (liquid nitrogen environment) demonstrated that the GSCC-based electrodes after 30 cycles at −40 °C exhibited a flat and stable electrode structure with uniform distribution of active materials and active sites (gallium and tin) at different voltages (Supplementary Figs. 37 and 38). Additionally, the GSCC-based batteries have stable ionic diffusion coefficients (Supplementary Fig. 39). This is due to the enhancement of ionic transport kinetics by the abundant polar groups of polymer, compensating for the reduced ionic conductivity of electrolyte in low-temperature region. When temperature increases to the liquid zone via the phase transition zone, the viscosity of LM decreases significantly, accompanied by a decrease in the interfacial impedance, indicating that the dynamic properties of LM are gradually restored. Besides, the interfacial wetting ability is enhanced. The coordination between polymer and LM can inhibit the aggregation tendency, stabilizing its homogeneous distribution in the electrode environment. In summary, the complementary strengths of the polymer and LM in GSCC provide high performance over the −40 °C to 60 °C temperature range, which effectively assists in the practical implementation of Li||S batteries in all-climate environments.

For supported active liquid metal electrocatalysts, the electrocatalytic activity depends on the distribution uniformity and loading stability on the carrier electrode[31]. However, in Li||S batteries, the large density difference between S and the SRR final product Li_2S leads to severe electrode volume changes, which in turn breaks electrode structures and result in a reduction in the electrocatalytic efficiency of the liquid metal due to aggregation/detachment. Therefore, a structure-modulated stable electrocatalytic mechanism was introduced by GSCC binder to ensure stable electrochemical performance over long cycles. In order to deeply investigate the stable electrocatalytic mechanism and demonstrate its advantages in the operating environment of Li||S batteries, a series of material characterization measurements were conducted. The state of GSCC electrodes under battery operation/open circuit is shown in Fig. 6a. In operating voltage range of 1.7–2.8 V, the liquid metal in GSCC exhibits spreading deformation due to the interfacial tension change caused by the surface electrochemical oxidation[53,54], the LM driven by electric field is able to connect the broken electron conduction paths within the microregion due to the improved dispersion. Also, the electrocatalytic efficiency is enhanced and can be used in conjunction with the high mechanical properties of GSCC to repair the microcracks in electrodes. The schematic diagram of the visualization device for exploring the electric field driven characteristics of LM in a battery-like operating condition is shown in Fig. 6b and Supplementary Fig. 40. The simplified cell simulating the battery's operating conditions was constructed by laying a carbon-coated aluminum foil collector at the bottom of the electrolytic cell and using a separator to separate the positive electrode from the negative electrode, and then applying drops of liquid metal to the surface of the collector. In the device, after applying voltage, the liquid metal still displays morphology changes (swelling, spreading) modulated by the electric field, which enables it to migrate toward the electrode-electrolyte interface during charging and discharging (Fig. 6c, Supplementary Fig. 41 and Supplementary Movie 1), thus providing dynamic active sites and regulating the interfacial contact. The separator avoids the migration and contact of liquid metal to the negative electrode, hence avoiding liquid metal shuttling and internal short circuits. Atomic force microscopy with applied surface potential (AFM-KPFM) was used to further probe the electric field-driven properties of LM droplets at the nanoscale (Fig. 6d and Supplementary Fig. 42). As the voltage increasing, the nanoscale LM droplets also produced tensile changes with the oxidation of the surface layer and showed swelling and spreading under the drive of the external electric field. Therefore, the nanoscale trace droplets in the close battery practical operating conditions can still realize the electric field driven and regulate the performance.

The abundant polar groups in GSCC can construct hydrogen bonding networks to provide a certain degree of self-healing ability while enhancing the electrocatalytic capability of LM through coordination. The good self-healing ability of GSCC samples was demonstrated by self-healing experiments (Supplementary Fig. 43a). The microscope images indicated that scratches on the surface of GSCC samples completely disappeared within 15 min. In temperature-variable FTIR tests, the stretching vibrational peaks of C=O, O-H and N-H blueshift to higher wavenumbers and the bending vibrational peaks of N-H redshift to lower wavenumbers with increasing temperature, which corresponds to the change of hydrogen bonding strengths in GSCC (Supplementary Fig. 44). In addition, the GSCC hydrogel exhibited favorable electronic conductivity and self-healing properties (Supplementary Fig. 43b). In conclusion, the working mechanism of the stable electrocatalytic ability of GSCC over a wide temperature range was explored through decoupling the material property variations, which also provides a feasible unique perspective for the development of advanced Li||S battery binders.

Discussion

In conclusion, this work prepares an electric field-driven binder GSCC with wide temperature adaptability through the composite of modified natural polymer and gallium-tin liquid metal. The short conjugated segments in GSCC amplify the advantage of liquid metal in

https://doi.org/10.1038/s41467-025-62909-1

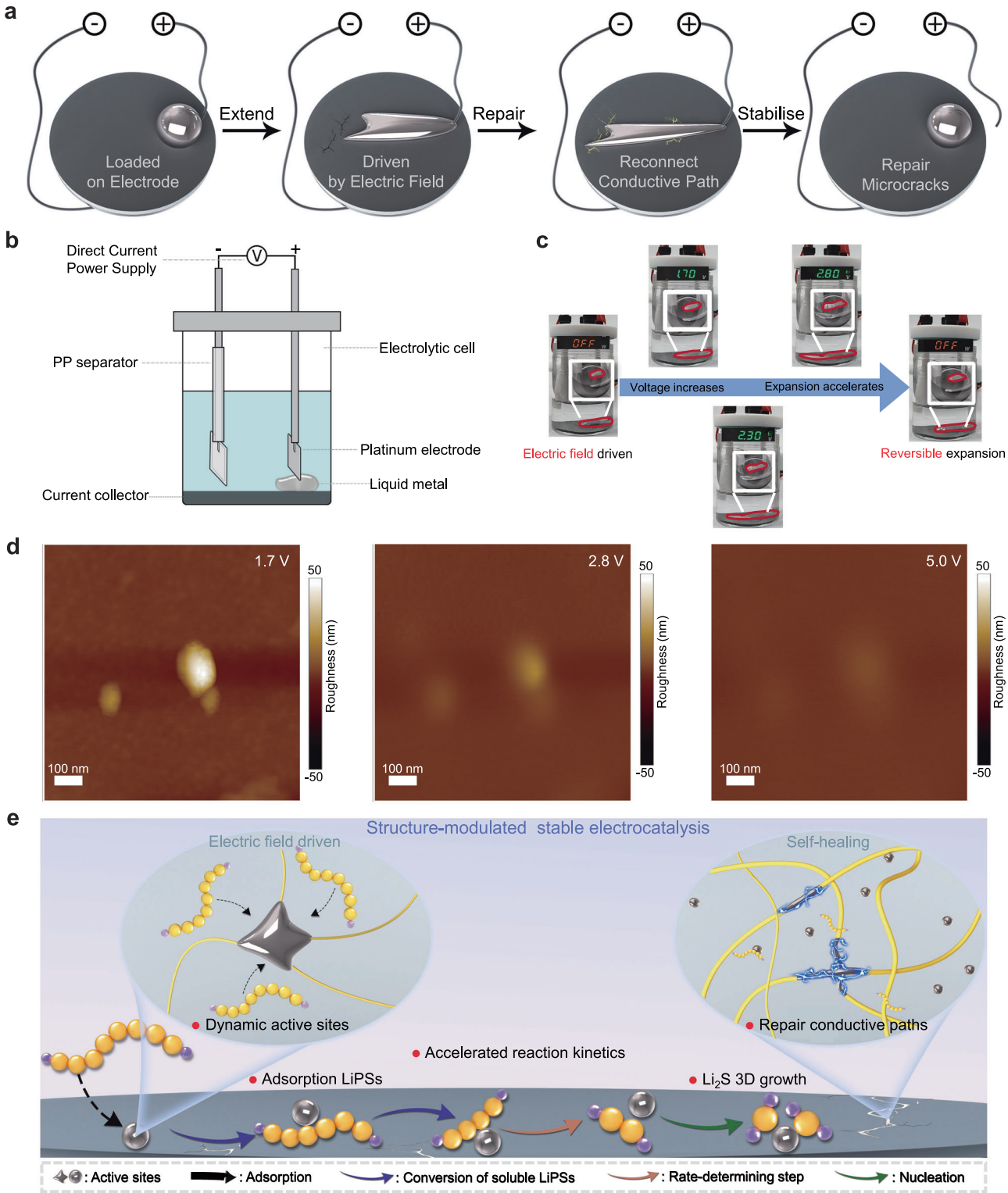

Fig. 6 | Electric field driven characteristics and self-healing ability of GSCC. **a** Schematic illustration of the electrode stabilization by the high mechanical strength of polymer network and the electric field driven properties of LM in GSCC binder. **b** Schematic diagram of electric field driven characteristic visualization device (**c**) Electric field driven characteristic visualization test in battery-like operating conditions (The inset figures show the direct current power supply connected to the device). **d** AFM of the LM at different voltages. **e** Schematic illustration of the stable electrocatalytic mechanism.

terms of its high electronic conductivity, while the coordination effect of polar groups and the electric field-driven property of liquid metal further enhance the electrocatalytic activity of GSCC. As a result, the binder has appropriate adsorption capacity for LiPSs and can catalytically accelerate their reaction kinetics over a wide temperature range. Also, the cycling performance and active material utilization of Li||S batteries are improved. After 500 cycles at 0.5 C (837.5 mA g^{-1}), the average capacity degradation rate of the batteries using GSCC is only 0.072%, and the specific capacity is still 470 mAh g^{-1} at the low temperature of −40°. Even at a high temperature of 60 °C, GSCC batteries

have a reversible capacity of 706.6 mAh g^{-1} at 0.5 C after 300 cycles. It worth to mention that the stable electrocatalytic mechanism of GSCC was explored, demonstrating its unique advantages in Li||S batteries. This work realizes the stable operation of Li||S batteries across a 100 °C temperature range solely by the innovative development of binder, which constitutes a promising strategy for the design of binders for practical wide temperature range Li||S batteries.

Methods

Materials

Chitosan (CTS, molecular weight: 600–800 kDa, about 90% deacetylated) was purchased from Thermo Scientific. 1,3-dioxane (DOL, Purity≥99.9%, Guaranteed Reagent), 1,2-dimethoxyethane (DME, Purity ≥ 99.9%, Guaranteed Reagent), and lithium sulfur commercial electrolyte (1 M LiTFSI in DME: DOL = 1:1 Vol% with 2%$LiNO_3$) were purchased from DoDoChem.Net. Caffeic acid (CA, Purity ≥ 99%), Morpholineethanesulfonic acid (MES, Purity ≥ 99.5%), N-Hydroxysuccinimide (NHS, Purity ≥ 98%), 1-(3-Dimethylaminopropyl)-3-ethylcarbodiimide methiodide (EDC, Purity ≥ 98%) and bis (trifluoromethyl sulfonyl) amine lithium salt (LiTFSI, Purity ≥ 99.9%) were purchased from Aladdin Reagent (Shanghai). Gallium-tin liquid metal is purchased from Shenyang Jiabei Company (its gallium to tin ratio is about 88:12). Lithium nitrate ($LiNO_3$, Purity ≥ 99.9%), Lithium sulfide (Li_2S, Purity ≥ 99.98%), and the other chemicals were purchased from Sigma-Aldrich (Shanghai). Graphene was purchased from Changzhou Sixth Element, sulfur powder (average particle size 50 nm), conductive agent Super P (powder conductivity 10–15 S cm^{-1}), and PVDF (relative molecular weight 900) were purchased from Guangdong Canrd New Energy Technology Co., Ltd. The carbon-coated aluminum foil (double-sided carbon coating, total thickness 18 μm) was purchased from Shenzhen Kejingzhida Technology Co., Ltd. The separator Canrd2325 was purchased from Guangdong Canrd New Energy Technology Co., Ltd. (PP, thickness 25 μm, lateral dimension 100 mm, porosity 39%, average pore size 0.028 μm, shaped into a circular form with a diameter of 19 mm prior to assembly in coin cells, with one sheet used per coin cell). Lithium discs and double-sided lithium-coated composite lithium strips were purchased from Guangdong Canrd New Energy Technology Co., Ltd. The lithium discs are circular with a diameter of 15.6 mm and a thickness of 0.45 mm, with a purity > 99.95%. The thickness of the lithium strips is: 50 μm lithium layers on both sides, with a 6 μm copper substrate in the middle. The lateral dimensions are: 90 mm for the lithium strip and 120 mm for the copper substrate, with the lithium strip centered (both were sealed and stored in a glove box at 25 °C filled with argon gas, where the long-term water and oxygen values were both <0.01 ppm, prior to use). The casing, spring, and gasket for coin cells are purchased from Shenzhen Kejingzhida Technology Co., Ltd. (positive and negative electrode casings are 2032, gasket diameter is 15.5 mm, thickness is 0.5 mm, spring diameter is 15.4 mm, height is 1.2 mm, and all materials are 304 stainless steel). Aluminum-plastic film was purchased from Guangdong Canrd New Energy Technology Co., Ltd. (thickness 113 μm, transverse dimension 200 mm). All chemical materials were used as received.

Preparation of caffeic acid modified chitosan (CC)

One gram chitosan was dissolved in 100 ml MES buffer solution (50 mM), and 0.6 ml HCl (12 mol/l) was added, then stirred for 0.5 h. 0.5405 g CA, 0.5751 g EDC, and 0.346 g NHS were added to a mixture of 100 ml anhydrous ethanol and 200 ml MES buffer solution with stirring for 1 h. The two solutions were subsequently mixed, and the pH was adjusted to 5.5, and the solution was stirred at 25 °C for 14 h under light protection. The solution was then dialyzed in deionized water for 48 h using a dialysis membrane (Mw = 1000), and a purified CC solution was obtained by vacuum filtration of the mixed solution, followed by freeze-drying to obtain CC.

Preparation of GSCC

In the preparation of GSCC, 0.2 g GaSn liquid metal was added to 100 ml CC solution (containing 0.8 g CC) and then homogeneously dispersed for 30 min under 800 W ultrasonic machine. The mixed solution was then rapidly frozen in liquid nitrogen and then freeze-dried for 72 h to obtain GSCC.

Preparation of carbon-sulfur (C-S) composite positive electrode

C-S composite materials are obtained by mixing sulfur with graphene in a mass ratio of 7:3, sealing the mixture in a Teflon-lined autoclave, and heating the autoclave in a muffle furnace at 155 °C for 12 h. C-S composite positive electrode slurry for coin batteries was prepared by mechanically mixing C-S composite powder (70 wt% S), conductive agent Super P, and polymer binder in a mass ratio of 7:2:1 in NMP. The mixing process of electrode slurry is conducted in a low-humidity dry room. The carbon-sulfur positive electrode is prepared by uniformly coating the mixed electrode slurry on one side of the carbon-coated aluminum foil using an automatic coating instrument (MSK-AFA-ES200) and then dried in a vacuum oven at 60 °C for 18 h. The slurry for pouch batteries was obtained by mechanically mixing C-S composite powder, conductive agent Super P, and polymer binder in a mass ratio of 8:1:1 in NMP. Subsequently, the pouch cell electrodes were prepared by applying the mixed electrode slurry to both sides of carbon-coated aluminum foil using an automatic coating machine (MSK-AFA-ES200). The electrodes were then dried in a vacuum oven at 60 °C for 24 h. The prepared electrodes are stored in an argon-filled glove box at 25 °C prior to use. For electrodes used in coin batteries, they are mechanically punched into circular electrodes (diameter = 11 mm) using a mechanical punch before assembly, and their mass is measured in an argon-filled glove box at 25 °C before use. For electrodes used in pouch cells, they were cut into rectangular electrodes with a length of 56 mm and a width of 43 mm using an electric cutting machine before assembly, with the tab positions retained. They were then weighed in an argon-filled glove box at 25 °C and welded with aluminum tabs for later use.

Electrode parameters

Coin cell. Surface sulfur loading in the electrode was 0.9–1.1 mg cm^{-2}, electrolyte volume/active material S (E/S ratio) was 12 μL mg^{-1}, no additives were used. The actual sulfur content in the positive electrode was 49 wt%, the actual carbon content was 41 wt% (20% for the conductive agent Super P and 21% for the carbon in the carbon-sulfur composite), and the actual binder content was 10 wt%.

High sulfur-loaded coin cell. Surface sulfur loading in the electrode was 5–6 mg cm^{-2} with an E/S ratio of 6–8 μL mg^{-1}, no additives were used. The actual sulfur content in the electrode was 49 wt%, the actual carbon content was 41 wt% (20% for the conductive agent Super P and 21% for the carbon in the carbon-sulfur composite), and the actual binder content was 10 wt%.

Pouch cell. Surface sulfur loading in the electrodes was 5–6 mg cm^{-2} with an E/S ratio of 7 μL mg^{-1}, no additives were used. The actual sulfur content in the electrodes was 56 wt%, the actual carbon content was 34 wt% (10% for the conductive agent Super P and 24% for the carbon in the carbon-sulfur composite), and the actual binder content was 10 wt%.

Preparation of Li_2S_8 electrolyte

Li_2S_8 electrolyte was prepared by adding *S* and Li_2S into DOL/DME (v/v = 1:1) solution at a mass ratio of 7:1 with continuous stirring for 36 h at 75 °C. The entire process was carried out in an argon-filled glove box at 25 °C, and the prepared Li_2S_8 solution was used for nucleation tests.

Preparation of Li_2S_6 electrolyte

To prepare Li_2S_6 solution, *S* and Li_2S were added in DOL/DME (v/v = 1:1) solution at a mass ratio of 5:1 and stirred continuously at 75 °C for 36 h. The entire process was carried out in an argon-filled glove box at 25 °C, and the Li_2S_6 solution was used for the visible adsorption experiments and symmetric battery tests.

Assembly of coin cells and pouch cells

The assembly of the coin cells is performed by sequentially placing the components from bottom to top: the stainless steel positive electrode battery case (2032 type), the pre-cut circular positive electrode, the commercial electrolyte (1 M LiTFSI in DME: DOL = 1:1 vol% with 2% $LiNO_3$, The pipette used is a 100 µl model.), the PP separator (a circular separator with a diameter of 19 mm made using a mechanical die-cutting machine), the Li metal negative electrode, stainless steel gasket, stainless steel spring, and negative electrode battery case. The coin cell is then placed with the negative electrode facing upward on the button cell sealing machine mold, and the pressure is adjusted and pressed for 5 s to complete the assembly of the button cell. The assembly of the pouch cell also employed a multi-layer superposition method. The pouch cell cathode with welded aluminum tabs was stacked with the PP separator and the lithium-coated copper foil with welded nickel tabs in a multi-layer configuration. This electrode stack was then enclosed within the aluminum-plastic film packaging material. Subsequently, the aluminum-plastic film was sealed using a sealing device, leaving only the tab side open for electrolyte injection (1 M LiTFSI in DME: DOL = 1:1 vol% with 2% $LiNO_3$). The pipette used is a 1000 µl model. After electrolyte injection, the pouch cell is placed in a vacuum environment to expel internal gases and achieve complete sealing. The entire process is conducted within an argon-filled glove box maintained at 25 °C.

Material characterization

^{1}H NMR spectra were detected by AVANCE NEO 600 M at room temperature. FTIR spectra and temperature-variable FTIR spectra were tested by Thermo Nicolet Nexus 470 FTIR spectrometer and Bruker EQUINOX55 infrared spectrometer, respectively. The chemical elemental analysis of the prepared products was obtained by XPS (ESCALAB250Xi). In situ Raman tests were performed on a Laser Micro-Raman Spectrometer (DXR Microscope). Viscosity rheology is tested by DHR-2. Scanning electron microscopy (SEM) was tested by the SEM5000. Low-temperature conditions SEM was tested by JSM-7610 Plus. Atomic force microscope (AFM) is tested by Bruker Dimension Icon, Germany.

Electrochemical measurements

Cyclic voltammetry (CV) tests (potential window 1.5–3 V) and Li_2S nucleation test were performed on a Biologic vpmp-3 multichannel workstation. The cycle performance and rate performance of the batteries were tested on the LAND-CT2001C and LAND-CT3002C test systems in a constant temperature chamber at 25 °C (MJS-SP250, with a temperature error of less than 1 °C). The high-temperature cycling performance of the batteries was tested in a sealed oven at 60 °C, and the low-temperature performance of the batteries was tested in a low-temperature constant temperature chamber (DW-60L30), with a temperature error of less than 1 °C during the testing process. Pouch cells require preload to be applied via external stainless steel fixtures during electrochemical tests, with the external pressure applied ~0.1 MPa. The variable-temperature impedance test (10 mHz–100 kHz) for the rate-determining step (from Li_2S_4 to Li_2S_2) was performed by PARSTAT MC, after discharging the cell to 2.0 V and stabilizing it at that potential for 30 min. In addition, the LAND-CT2001C and LAND-CT3002C instruments were used for the GITT tests, performed by alternating 20-min constant current pulses (0.1 C, 167.5 mA g^{-1}) and open-circuit voltage (OCV) periods (20 min).

Diffusion coefficient of Li^+: The D_{Li^+} is calculated by interpolating the results of GITT tests according to the following equation derived from Fick's second law:

$$D_{Li}^{+} = \frac{4}{\pi\tau}\left(\frac{n_m V_m}{S}\right)^2\left(\frac{\Delta E_s}{\Delta E_\tau}\right)^2$$

where τ represents the duration of the current pulse n_m and V_m denote the mole number and molar volume of the positive electrode materials, respectively. *S* is the contact area between electrolyte and electrodes. ΔE_s and ΔE_τ refer to the change of the steady-state potential at the end of the relaxation period over a single galvanostatic titration and the total change of battery potential during a constant current pulse, respectively.

Adsorption experiments

The same mass (40 mg) of PVDF and GSCC was added to 10 ml of diluted 1 mM Li_2S_6 solution, respectively. The color of the solution was recorded after 48 h of standing and the residual polymer was removed by filtration using a small filter. The clear solution was used for Ultraviolet–visible (UV–vis) test, while the filtered polymers were washed with a blank electrolyte (DME: DOL = 1:1 vol%) and used for XPS test. All the above adsorption experiments and subsequent processing were conducted in an argon-filled glove box at 25 °C.

Li_2S nucleation test

The test electrode was prepared by mixing graphene and polymer binder in a mass ratio of 7:3 to form an electrode slurry, which was then coated on carbonized aluminum foil and dried in a vacuum oven at 60 °C for 48 h. The electrode was punched into a 11 mm diameter disc and assembled into a coin cell with lithium metal (negative electrode), Canrd2325 (separator), and 20 µL of 0.2 M Li_2S_8 (electrolyte) as the positive electrode. For nucleation tests at 25 °C, the batteries were galvanostatically discharged to 2.09 V with a current of 0.2 mA and potentiostatically discharged at 2.08 V until the current dropped below 0.01 mA. For nucleation tests at 0 °C, the batteries were galvanostatically discharged to 2.03 V with a current of 0.2 mA and potentiostatically discharged at 2.02 V until the current dropped below 0.01 mA.

EIS tests

For EIS tests on rate-determining step batteries, Li||S batteries based on different binders were uniformly discharged to 2.0 V in constant current mode (0.2 mA) before testing and maintained for 30 min to stabilize the potential. Subsequently, within the frequency range of 10 mHz to 100 kHz, the signal amplitude is set to 10 mV RMS, the constant potential signal is set (with the set potential relative to the open-circuit voltage at 2.0 V), and the number of data points is set to 10 points per decade of frequency.

Visualization test of electric field driven characteristics

A simplified cell that simulates the battery operating conditions was constructed by laying a charcoal-coated aluminum foil collector at the bottom of the electrolytic cell and separating the positive electrode and negative electrode using a separator (separator wrapped around the negative electrode), and then applying drops of liquid metal to the surface of the collector. Subsequently, the device was connected to a direct current power, and the electric field driving characteristics were visualized and tested in a battery-like environment by applying a voltage through it (the voltage in the operating range of Li||S batteries, 1.7–2.8 V).

Density functional theory calculation

Density functional theory (DFT) calculations were performed using Gaussian and the Vienna Ab initio Simulation Package (VASP). The frontier molecular orbitals (HOMO and LUMO) of the polymer CC and CTS were extracted and analyzed from the formatted checkpoint files (.fchk) generated by Gaussian. All geometric structures were fully optimized, and the corresponding energies were calculated at the B3LYP/6-31 + G(d,p) level of theory. The calculation parameters and detailed files for HOMO-LUMO are available in Supplementary Data 1. To reflect the liquid and dynamic nature of liquid metal, the computational model of GSCC was constructed by combining the liquid metal in the form of clusters of atoms with a Ga/Sn atomic ratio of 27:3 with the polymerized units of caffeic acid modified chitosan (CC), and sufficient structural relaxation was carried out. Density of states (DOS), differential charge density, adsorption energies, and Gibbs free energy of various materials were calculated by density functional theory calculations via the VASP[55]. The calculation parameters and detailed files for density of states calculations and differential charge density are available in Supplementary Data 2 and 3. The calculations utilized the projector augmented-wave (PAW) method[56] and the Perdew-Burke-Ernzerhof (PBE) functional[57] within the framework of the Generalized Gradient Approximation (GGA). The energy cutoff was set to 500 eV, with a energy convergence criterion of $1.0e^{-5}$ eV and a force convergence criterion of −0.02 eV $Å^{-1}$. The Gibbs free energy of reaction was computed using the DMol3 module in Materials Studio[58], with the global orbital cutoff set to 3.3 Å and a total energy convergence criterion of $1.0e^{-5}$ Hartree.

During catalytic reactions, the Gibbs free energy ΔG was defined as the difference in free energy between each step and the initial and final states, expressed as:

$$\Delta G = \Delta E + \Delta ZPE - T\Delta S$$

where ΔE is the adsorption energy of reactant and product molecules on the catalyst surface; ΔZPE and ΔS are the changes in zero-point energy and entropy caused by the reaction, which can be obtained by calculating the vibrational frequencies to determine the changes in zero-point energy and entropy at room temperature.

Data availability

The data supporting the findings of this work are available within the article and its Supplementary Information files. Source Data are provided with this paper. All other relevant data supporting the findings of this study are available from the corresponding author on request. Source data are provided with this paper.

References

1. Bruce, P. G., Freunberger, S. A., Hardwick, L. J. & Tarascon, J. M. Li-O_2 and Li-S batteries with high energy storage. *Nat. Mater.* **11**, 19 (2011).
2. Armand, M. & Tarascon, J. M. Building better batteries. *Nature* **451**, 652 (2008).
3. Manthiram, A. et al. Rechargeable lithium–sulfur batteries. *Chem. Rev.* **114**, 11751 (2014).
4. Liu, R.-L. et al. Establishing reaction networks in the 16-electron sulfur reduction reaction. *Nature* **626**, 98 (2024).
5. Yao, X. M. et al. In situ interweaved high sulfur loading Li-S cathode by catalytically active metalloporphyrin based organic polymer binders. *Adv. Mater.* **35**, 2208846 (2023).
6. Chung, W. J. et al. The use of elemental sulfur as an alternative feedstock for polymeric materials. *Nat. Chem.* **5**, 518 (2013).
7. Zhang, H., Li, Y., Pana, L. & Sun, Z. M. MXene-derived Ti_nO_{2n-1} quantum dots distributed on porous carbon nanosheets for stable and long-life Li-S batteries: enhanced polysulfide mediation via defect engineering. *Adv. Mater.* **33**, 2008447 (2021).
8. Wang, N. N. et al. Thickness-independent scalable high-performance Li-S batteries with high areal sulfur loading via electron-enriched carbon framework. *Nat. Commun.* **12**, 4519 (2021).
9. Zhang, H. et al. Lithium–sulfur pouch cells with 99% capacity retention for 1000 cycles. *Energy Environ. Sci.* **17**, 7047 (2024).
10. Chen, Y. et al. Advances in lithium-sulfur batteries: from academic research to commercial viability. *Adv. Mater.* **33**, 2003666 (2021).
11. Li, Y. D. et al. Bowling collision effect" of CoMo6 polyoxometalate units enables wide temperature range from −20 to 60 °C and dendrite mitigation Li-S batteries. *Adv. Mater.* **36**, 2406343 (2024).
12. Zhou, Z. F., Li, G. C., Zhang, J. J. & Zhao, Y. F. Wide working temperature range rechargeable lithium–sulfur batteries: a critical review. *Adv. Funct. Mater.* **31**, 2107136 (2021).
13. Peng, L. L. et al. A fundamental look at electrocatalytic sulfur reduction reaction. *Nat. Catal.* **3**, 762 (2020).
14. Ji, X., Lee, K. T. & Nazar, L. F. A highly ordered nanostructured carbon–sulphur cathode for lithium–sulphur batteries. *Nat. Mater.* **8**, 500 (2009).
15. Zhang, Z. Q. et al. A multifunctional graphene oxide-Zn (II)-triazole complex for improved performance of lithium-sulfur battery at low temperature. *Electrochim. Acta* **271**, 58 (2018).
16. Shi, F. Y. et al. Stable liquid-sulfur generation on transition-metal dichalcogenides toward low-temperature lithium–sulfur batteries. *ACS Nano* **16**, 14412 (2022).
17. Ji, H. Q. et al. Weakening Li^+ de-solvation barrier for cryogenic Li-S pouch cells. *Adv. Mater.* **35**, 2208590 (2023).
18. Guo, Y. C. et al. Regulating adsorption ability toward polysulfides in a porous carbon/Cu3P hybrid for an ultrastable high-temperature lithium-sulfur battery. *Carbon Energy* **3**, 841 (2021).
19. Guo, D. et al. Electrolyte engineering for thermally stable Li-S batteries operating from −20 °C to 100 °C. *Energy Environ. Sci.* **17**, 8151 (2024).
20. Wang, S. et al. Polythiocyanogen as cathode materials for high temperature all-solid-state lithium-sulfur batteries. *ACS Energy Lett.* **8**, 2699 (2023).
21. Gao, X. J. et al. Cobalt-doped SnS_2 with dual active centers of synergistic absorption-catalysis effect for high-S loading Li-S batteries. *Adv. Funct. Mater.* **29**, 1806724 (2019).
22. Cai, G. L. et al. A volcano correlation between catalytic activity for sulfur reduction reaction and Fe atom count in metal center. *J. Am. Chem. Soc.* **146**, 13055 (2024).
23. Yang, Q. et al. Chlorine bridge bond-enabled binuclear copper complex for electrocatalyzing lithium-sulfur reactions. *Nat. Commun.* **15**, 3231 (2024).
24. Ci, H. et al. Defective VSe_2-graphene heterostructures enabling in situ electrocatalyst evolution for lithium-sulfur batteries. *ACS Nano* **14**, 11929 (2020).
25. Song, X. Q. et al. Accelerating sulfur redox reactions by topological insulator Bi_2Te_3 for high-performance Li-S batteries. *Adv. Funct. Mater.* **32**, 2109413 (2022).
26. Taccardi, N. et al. Gallium-rich Pd-Ga phases as supported liquid metal catalysts. *Nat. Chem.* **9**, 862 (2017).
27. Seo, Y. et al. Graft copolymer-stabilized liquid metal nanoparticles for lithium-ion battery self-healing anodes. *Adv. Funct. Mater.* https://doi.org/10.1002/adfm.202508062 (2025).
28. Qi, Y. Q. et al. Dynamic liquid metal catalysts for boosted lithium polysulfides redox reaction. *Adv. Mater.* **34**, 2204810 (2022).
29. Tang, J. et al. Molten Sn solvent expands liquid metal catalysis. *Nat. Commun.* **16**, 907 (2025).
30. Li, G. et al. Chemisorption of polysulfides through redox reactions with organic molecules for lithium-sulfur batteries. *Nat. Commun.* **9**, 705 (2018).

31. Fatima, S. S. et al. Current state and future prospects of liquid metal catalysis. *Nat. Catal.* **6**, 1131 (2023).
32. Huang, Y. Y. et al. A saccharide-based binder for efficient polysulfide regulations in Li-S batteries. *Nat. Commun.* **12**, 5375 (2021).
33. Haque, A. B. M. T. et al. Electrically conductive liquid metal composite adhesives for reversible bonding of soft electronics. *Adv. Funct. Mater.* **34**, 2304101 (2024).
34. Kim, J. H. et al. Regulating electrostatic phenomena by cationic polymer binder for scalable high areal-capacity Li battery electrodes. *Nat. Commun.* **14**, 5721 (2023).
35. Senthil, C., Kim, S.-S. & Jung, H. Y. Flame retardant high-power Li-S flexible batteries enabled by bio-macromolecular binder integrating conformal fractions. *Nat. Commun.* **13**, 145 (2022).
36. Cheng, B. et al. Ultrastrong underwater adhesion on diverse substrates using non-canonical phenolic groups. *Nat. Commun.* **13**, 1892 (2022).
37. Yang, K. et al. Constructing a highly efficient aligned conductive network to facilitate depolarized high-areal-capacity electrodes in Li-ion batteries. *Adv. Energy Mater.* **11**, 2100601 (2021).
38. Gréa, T. et al. Subcutaneous administration of a zwitterionic chitosan-based hydrogel for controlled spatiotemporal release of monoclonal antibodies. *Adv. Mater.* **36**, 2308738 (2024).
39. Fu, M. N. et al. Optimizing Na plating/stripping by a liquid sodiophilic Ga-Sn-In alloy towards dendrite-poor sodium metal anodes. *Energy Storage Mater.* **63**, 103020 (2023).
40. Jin, X. et al. Micro-stress pump with variation of stress to boost the ion transport for high-performance sodium ion batteries. *Energy Environ. Sci.* **17**, 7035 (2024).
41. Lin, L. et al. A semi-conductive organic cathode material enabled by extended conjugation for rechargeable aqueous zinc batteries. *Energy Environ. Sci.* **16**, 89 (2023).
42. Tian, S. H. et al. Multi-dimensional composite frame as bifunctional catalytic medium for ultra-fast charging lithium-sulfur battery. *Nano Micro Lett.* **14**, 196 (2022).
43. Cao, Y. et al. Fucoidan cross-linking polyacrylamide as multifunctional aqueous binder stabilizes $LiCoO_2$ to 4.6 V. *Adv. Funct. Mater.* **34**, 2405911 (2024).
44. Han, Z. Y. et al. Machine-learning-assisted design of a binary descriptor to decipher electronic and structural effects on sulfur reduction kinetics. *Nat. Catal.* **6**, 1073 (2023).
45. Fan, X.-M. et al. Surface modification engineering enabling 4.6 V single-crystalline Ni-rich cathode with superior long-term cyclability. *Adv. Funct. Mater.* **32**, 2109421 (2022).
46. Deng, D.-R. et al. Accelerating the rate-determining steps of sulfur conversion reaction for lithium-sulfur batteries working at an ultrawide temperature range. *Adv. Mater.* **36**, 2406135 (2024).
47. Li, B. et al. 3D adsorption-mediator network polymer binders improve redox kinetics and flame retardant performance for high loading lithium-sulfur batteries. *Adv. Funct. Mater.* **33**, 2306990 (2023).
48. Zhang, H. et al. Wang, Operating lithium-sulfur batteries in an ultrawide temperature range from −50 °C to 70 °C. *Adv. Funct. Mater.* **33**, 2304433 (2023).
49. Cai, G. et al. Solvent selection criteria for temperature-resilient lithium–sulfur batteries. *Proc. Natl. Acad. Sci. USA* **28**, 119 (2022).
50. Zhao, C. et al. Pushing lithium-sulfur batteries towards practical working conditions through a cathode-electrolyte synergy. *Angew. Chem.* **134**, e202203466 (2022).
51. Ma, L. B. et al. Wide-temperature operation of lithium-sulfur batteries enabled by multi-branched vanadium nitride electrocatalyst. *ACS Nano* **17**, 11527 (2023).
52. Liao, K., Pai, M. H. & Manthiram, A. Tuning the solvation structure of a weakly solvating cyclic ether electrolyte for wide-temperature cycling of lithium-sulfurized polyacrylonitrile batteries. *Adv. Energy Mater.* **15**, 2403733 (2024).
53. Suo, J. et al. A novel super-toughness and self-healing solid polymer electrolyte for solid sodium metal batteries. *Adv. Mater.* **36**, 2409587 (2024).
54. Shen, Y. F. et al. Reactive wetting enabled anchoring of non-wettable iron oxide in liquid metal for miniature soft robot. *Nat. Commun.* **14**, 6276 (2023).
55. Kresse, G. & Furthmüller, J. Efficient iterative schemes for ab initio total-energy calculations using a plane-wave basis set. *Phys. Rev. B* **54**, 11169 (1996).
56. Blöchl, P. E. Projector augmented-wave method. *Phys. Rev. B* **50**, 17953 (1994).
57. Perdew, J. P., Burke, K. & Ernzerhof, M. Generalized gradient approximation made simple. *Phys. Rev. Lett.* **77**, 3865 (1996).
58. Delley, B. An all-electron numerical method for solving the local density functional for polyatomic molecules. *J. Chem. Phys.* **92**, 508 (1990).

Acknowledgements

The authors acknowledge the support from Scientific Research Innovation Capability Support Project for Young Faculty (ZYGXQNJSKYCXNLZCXM-M4), National Outstanding Youth Science Fund (52222314), CNPC Innovation Found (2021DQ02-1001), Dalian Outstanding Youth Science and Technology Talent Project (2023RJ006), Dalian Science and Technology Innovation Project (2022JJ12GX022).

Author contributions

F.H., X.-G.J., and W.J. conceived and designed the idea. T.Z. and W.J. designed the experiments. W.J. synthesized the polymer binder with T.Z.'s guidance. W.J., B.L. and Y.Q. performed characterization of the materials and tests of the Li||S batteries. X.J., W.J., and L.W. discussed and analyzed the data. C.S. and M.P. performed the theoretical simulations. W.J. wrote the manuscript and all authors commented on the manuscript. All authors have given approval to the final version of the manuscript.

Competing interests

The authors declare no competing interests.

Additional information

Supplementary information The online version contains supplementary material available at https://doi.org/10.1038/s41467-025-62909-1.

Correspondence and requests for materials should be addressed to Tianpeng Zhang, Xigao Jian or Fangyuan Hu.

Peer review information *Nature Communications* thanks Karma Zuraiqi, Shan Liu and the other, anonymous, reviewer(s) for their contribution to the peer review of this work. A peer review file is available.

Reprints and permissions information is available at http://www.nature.com/reprints

Publisher's note Springer Nature remains neutral with regard to jurisdictional claims in published maps and institutional affiliations.

Open Access This article is licensed under a Creative Commons Attribution-NonCommercial-NoDerivatives 4.0 International License, which permits any non-commercial use, sharing, distribution and reproduction in any medium or format, as long as you give appropriate credit to the original author(s) and the source, provide a link to the Creative Commons licence, and indicate if you modified the licensed material. You do not have permission under this licence to share adapted material derived from this article or parts of it. The images or other third party material in this article are included in the article's Creative Commons licence, unless indicated otherwise in a credit line to the material. If material is not included in the article's Creative Commons licence and your intended use is not permitted by statutory regulation or exceeds the permitted use, you will need to obtain permission directly from the copyright holder. To view a copy of this licence, visit http://creativecommons.org/licenses/by-nc-nd/4.0/.

© The Author(s) 2025